Conf-7712 40--1

APPLICATION OF PROTON RADIOGRAPHY TO MEDICAL IMAGING

S. L. Kramer, R. L. Martin, D. R. Moffett, and E. Colton

Prepared for

First International Seminar on the Use of
Proton Beams in Radiation Therapy
Moscow, USSR
December 1977

UofC-AUA-USDOE

ARGONNE NATIONAL LABORATORY, ARGONNE, ILLINOIS

Operated under Contract W-31-109-Eng-38 for the
U. S. DEPARTMENT OF ENERGY

Application of Proton Radiography to Medical Imaging*

S. L. Kramer, R. L. Martin, D. R. Moffett, and E. Colton
Argonne National Laboratory
Argonne, Illinois U.S.A.

Abstract

The use of charged particles for radiographic applications has been considered for some time, but progress has been impeded by the cost and availability of suitable accelerators. However, recent developments in technology could overcome these problems. We, therefore, present a review of the physical principles leading to an improvement in mass resolution per unit of absorbed dose for charged particle radiography relative to x-ray radiography. The quantitative comparisons between x-ray and proton radiographs presented here confirm this advantage. The implications of proton radiography on cancer detection and therapy, as well as future plans for developing a proton tomographic system, are discussed.

Introduction

Very shortly after the discovery of x-rays this radiation was employed for medical radiography. Since then, numerous improvements in medical imaging have resulted from technological developments, but the basic physical principles have remained unchanged. Despite these advances, two major problems still face x-ray imaging: high exposure dose and lack of resolution for soft tissue structure. The possibility of using protons for radiographic imaging was suggested some time ago.[1] Several attempts[2-5] to demonstrate that heavy charged particles could overcome the shortcomings of x-ray radiography have been performed. However, despite these attempts, charged particle radiography has not progressed rapidly due primarily to source availability and cost.

---

*Work supported by the U.S. Department of Energy and the National Cancer Institute through Contract No. NO1-CB-43918.

At Argonne National Laboratory, we have recognized the advantages of proton radiography, as well as the problems which need to be overcome in turning this novel idea into a practical procedure. In this paper, we will present a rather simplified description of the physical basis for charged particle radiography together with some preliminary data taken to justify these claims. Also included is a brief description of our future plans toward developing a clinically practical radiographic system.

Physics of Charged Particle Radiography

As a monoenergetic beam of charged particles passes through matter, it experiences frequent but gentle (small energy loss) collisions with the atomic electrons. These collisions produce a gradual deceleration of these particles until they come to rest after penetrating a definite thickness. Since each collision can produce a range of energy transfer to the atomic electrons, not all particles lose energy at exactly the same rate but they have a spread about a statistical mean, resulting in a straggling of the range about a well defined average value. The particle attenuation distribution is well described by a gaussian distribution with an rms spread of ranges (σ) about the average range (R). For the energy range required for human radiography and for biological material, σ is approximately proportional to R as follows:

$$\sigma/R \approx 0.01\ A^{-1/2} \qquad (1)$$

where A is the atomic mass of the charged particle being used.[6]

In addition to the gradual deceleration of the particles, infrequent nuclear collisions occur and cause attenuation of the primary beam. For protons of 200 MeV, the attenuation rate in biological tissue is about 1.2% per g/cm^2. For other incident particles with atomic mass, A, the attenuation rate is given by

$$\Sigma = 0.45\ (A^{1/3} + M^{1/3} - 1.2)^2\%\ \text{cm}^2/\text{g}$$

where M is the effective atomic mass of the material being penetrated. Therefore, carbon ions will attenuate about three times faster than protons.

Figure 1 shows the transmission curve for 200 MeV protons in water, including the effect due to nuclear interactions. For comparison, the transmission curve for a 40 keV x-ray beam is also plotted. Comparison of these two curves clearly indicates the physical basis for charged particle radiography. Using the steep part of the proton transmission curve, one needs to measure changes in transmission less accurately than for x-rays to detect a given change in thickness or mass. Quantitatively, the mass resolution for a radiographic exposure is given by

$$\delta = \frac{\Delta}{|dT/dx|} \tag{2}$$

where dT/dx is the slope of the transmission curve and Δ is the accuracy of the transmission measurement. For measurements not dominated by instrumentation accuracy or quantum inefficiency, the statistical accuracy of the transmission measurement is $\Delta \propto 1/\sqrt{N_o}$, where N_o is the incident flux of particles. It can then be shown that the flux of protons (N_p) required to yield the same mass resolution as a given flux of x-rays ($N\gamma$) is

$$N_p = 2\pi\sigma^2\mu^2 e^{-\mu x} N_\gamma \tag{3}$$

where μ is the x-ray attenuation coefficient. It should be noted that this equation does not include nuclear interactions, a small correction for protons but more significant for heavier ions, nor does it include the polychromatic nature of x-rays and the variation of μ with energy. For the example shown in Fig. 1, the flux reduction for x-rays is 2.1×10^{-5}, an order of magnitude smaller than the increased energy (i.e., average dose) required for protons over that for x-rays. More detailed calculations[7] show a reduction of average dose of 8 to 16 with an additional factor of four reduction in peak dose, provided sufficient proton energy is used to absorb the Bragg peak in the detector rather than in the patient.

Because of the slowing down of the charged particles, the transmission curve in effect measures the stopping power (i.e., linear energy transfer or MeV/g/cm^2) of the material. The stopping power is to a very good approximation proportional to the

electron density or the effective Z/A of the material.[8] Therefore, aside from changes in hydrogen concentration, charged particle radiography dominantly measures changes in mass density rather than changes in chemical composition. Figure 2 shows the stopping power for protons at 100 and 200 MeV as a function of the Z of the material. Except for hydrogen, the spread in stopping power around the average is about 10% over the biological elements. As shown by the curve in Fig. 2, some of the changes in stopping power are the result of variations in Z/A from 1/2. For x-rays, the change in the mass attenuation coefficient over this same range is a factor of 10 for 40 keV and a factor of two for 100 keV, as shown in Fig. 3. Consequently, changes in heavy element composition are more important for x-ray radiography than for charged particles. For example, the ratio of mass attenuation for bone to muscle is a factor of two for 40 keV x-rays[9] compared to a factor of 0.9 for the ratio of proton stopping power.[10] This property of charged particles, together with the improved mass resolution, could prove very useful in detecting tumors within soft tissue.[2]

One problem with charged particle radiography that has caused concern is the beam spread due to multiple coulomb scattering in the radiographed object. This effect would produce blurring of the image of several millimeters for protons, depending on the object-to-detector distance. Although little improvement of this blurring is possible for shadowgraph imaging, without sacrificing the dose advantage (e.g., using heavy ions or collimating the detector), the effect of this blurring can be greatly reduced for tomographic imaging. If the beam position and angle are accurately known for the incident and exiting beam, then the accuracy of the ray which these particles followed in passing through the object can be known to about 1 mm for protons.[11] Therefore, the geometrical resolution for proton computerized axial tomographic (CAT) scanning can be comparable to existing x-ray scanners,[12] with further improvements possible by using heavier ions or additional correction techniques. As will be described, improvement

of the geometrical resolution is the only real advantage that heavy ions have over protons.

The use of heavy ions for radiography has been considered by several investigators[4,5] not only for their reduced multiple scattering but also for a reputed improvement in the dose. Equations (1) and (3) indicate that the reduced range straggling for heavy ions results in a reduction of particle flux proportional to A for a given mass resolution. However, the energy required to penetrate a given thickness increases as

$$E \propto Z^{1.12} A^{0.44} \qquad (4)$$

where Z and A are the atomic number and mass of the ion, respectively, and we have used an approximation to the range energy relation for protons of $E \propto R^{0.56}$. Equations (1), (3) and (4) indicate that for a 26 cm object and helium ions, the mass resolution per unit of dose should be equal to that for protons, while carbon ions suffer a factor of 1.9 more dose for the same resolution. Not included in this comparison is the increased beam attenuation due to nuclear interactions which actually results in a 20% increased dose for helium ions. For carbon ions, the total increase in dose is about 4.5 compared to that for protons for the same density resolution. In addition to this increase in average dose is a somewhat larger RBE for heavy ions as compared to protons, RBE $\approx$ 1.0 for protons of the required energy.[13] This is to be compared with an entrance RBE $\approx$ 2.0 for carbon ions[14] of sufficient energy to penetrate 26 cm of H_2O.

Some reduction of the absorbed dose ($\approx$ 30%) and of the multiple scatter smearing ($\approx$ 40%) is possible by using deuterium or tritium ions, but not without some increase in accelerator costs for the higher energies required. Therefore, we conclude that protons have the greatest potential for development into a practical radiographic procedure.

Recent Experimental Results

In order to demonstrate the advantages of protons over x-rays, an experiment[15] was performed at Argonne National Laboratory using the 200 MeV beam from the Booster I synchrotron. This accelerator provided 10^{11} protons in 100 nsec pulses at a rate of 15 pulses/sec. Figure 4 shows the beam transport and collimation system used to produce four 1 mm^2 beams separated vertically by 64 mm. Each beam had an intensity of about 5000 protons/pulse. Specimens to be radiographed were placed in a 23 cm long water box with parallel sides and stepped horizontally across the beams at the rate of 15 mm/sec. At the end of each horizontal scan, the box was lowered 1 mm and the horizontal scan repeated in the opposite direction. A complete 254 mm x 254 mm scan required about 18 min.

The beam intensity upstream and downstream of the specimen box was measured using plastic scintillators coupled to photomultiplier tubes. The signals from the eight counters were integrated, digitized, and written on magnetic tape along with the scan coordinates and other parameters.

Analysis of the data was done on an off-line computer where the ratio of the downstream to upstream signal was computed to yield the fraction of transmitted flux (T). Figure 5 presents the transmitted flux for each of the four beams from a single horizontal scan of a phantom with holes of different contrast. Beams 1 and 2 scan only the water bath, beam 3 scans through the center of the 1/4 in. diameter holes, and beam 4 scans only the uniform area of the phantom. Immediately obvious from these data is the lack of adequate energy stability from the accelerator, which produces a change in transmission as the result of a change in the range of the protons. The oscillating signal observed in Fig. 5 results from $\pm$ 0.3% fluctuations of the beam energy. Although this stability is adequate for nuclear physics experiments, it is disastrous for radiological applications. To overcome this effect, beam 1 was made to always scan only the uniform water box (if possible) and the energy fluctuations measured by this beam

were used to correct the others. Figure 6 shows the same scan lines shown in Fig. 5 but with the energy corrections made. The resulting scan clearly shows six of the seven holes scanned by beam 3 with a decrease in contrast from one hole to its neighbor of a factor of two from right to left. The sixth hole has a change in the integrated mass of 0.13% from the background, slightly greater than the measured statistical noise. The rms noise was measured by determining the variance about the mean for 100 data points in a uniform section of the phantom. The rms noise was about 0.1% in mass or about a factor of five worse than expected from quantum statistics. This was due to instrumentation resolution of about 1% in transmission, which would have yielded a 0.07% mass resolution if the energy corrections were not necessary. While scanning the specimen box with only water in it, a decrease in mass of the lower lefthand corner of the box with respect to the upper righthand corner was observed, corresponding to a 0.008 in. misalignment. This nonuniformity of the box will be visible in all shadowgraph displays presented here, when shown with a narrow display window.

Figure 7 shows the proton shadowgraphs of the phantom discussed previously. This phantom is similar to that developed by Burger[16] for x-ray perception studies. It consists of a block of mylar (3 cm thick) with five rows of seven holes drilled in it. Each row of the phantom has holes of constant diameter varying in steps of a factor of two from 0.5 in. to 0.031 in. from top to bottom respectively, and each column has holes of constant contrast (length) varying in steps of a factor of two from 4.2% to 0.07% from right to left, respectively. In the shadowgraph in Fig. 7, each scan position is represented by a shaded picture element or pixel. The darker the pixel, the greater the mass measured by the proton beam. Figure 7(c) has the narrowest range of mass in the display window (1.5-1.7 g/cm^2), and the statistical noise is clearly evident. Although the reproduction of Fig. 7 leaves something to be desired, the original display clearly indicated that the seventh hole is visible in the 0.5 in. diameter row. Figure 8 presents the minimum contrast or length of hole (L) visible as a

function of the hole diameter (D). The curve is an attempt to describe these data assuming a constant signal-to-noise ratio (LD) modified by the effective beam size (b ≈ 0.6 mm) as follows:

$$LD[D/(D + b)]^2 = \text{constant} . \quad (5)$$

For comparison, Fig. 9 shows the shadowgraph of the same phantom taken with x-rays using Kodak RPRO screen film. Although the spatial resolution is markedly better for the x-ray shadowgraph (proton shadowgraph is limited by finite beam size), the mass resolution is comparable to that obtained with protons except that the x-ray radiograph seems to have a minimum detectable contrast due to scattered radiation or fogging of the film. Figure 10 shows the visibility data obtained from the x-ray shadowgraph in Fig. 9, with the contrast threshold evident. A more detailed study of x-ray resolution was performed by Burger,[16] and his results (curve in Fig. 10) supported the presence of this minimum detectable contrast. There are obvious ways to improve the limitations of the x-ray shadowgraph imposed by scattered radiation (e.g., employing grids or similar scanning beams), and this work is in progress.

The proton shadowgraph in Fig. 7 was taken through 24 cm of water with a 75 mrads back surface dose, while the x-ray shadowgraph in Fig. 9 was taken only through the 3 cm phantom and had a front surface dose of about 300 mrads. However, the dose for the proton shadowgraph could have been reduced a factor of 25 without causing a significant change in the visibility curve (Fig. 8) since the noise was limited by instrumentation accuracy and not by quantum statistics.

In Fig. 11, we present a proton mammograph of a radical mastectomy with the breast placed in a 4 in. thick water box and the beam energy reduced to 147 MeV. In the upper lefthand corner, the increased density is due to muscular tissue and considerable hemorrhaging. In this region, numerous stainless steel clips, used to control the hemorrhaging, are clearly visible. The nipple is located in the lower righthand corner, and the site of the original biopsy is located in the lower central region. On the lefthand

side of the radiograph near the center is a region of increased density. Pathology indicated that several lymph nodes of 0.5 to 2.5 cm in size were "grossly replaced by firm white neoplastic tissue" in this region. Figure 12 shows an x-ray mammograph of the same breast in the same water box. The x-ray was taken in two pieces and spliced together afterwards. The structure visible in the proton radiograph is visible in the x-ray with considerably better spatial detail, a limitation due partly to the 1 mm proton beam size and partly to the multiple scattering. The estimated front surface dose for the x-ray radiograph was about 4 rads compared to a back surface dose of 75 mrads for the proton radiograph. However, as described before, the proton dose could have been reduced a factor of 25 without seriously effecting the mass resolution.

Future Possibilities for Proton Radiography

A major impediment to considering proton radiography as a practical diagnostic tool has been the cost of the proton source. However, the preliminary design of a synchrotron capable of providing a beam adequate for radiographic applications at a reasonable cost has been proposed.[17] This accelerator could provide beam to several diagnostic rooms, thereby further reducing the unit cost for large installations. It, therefore, remains to be demonstrated that a practical tomographic system with protons can be developed which retains this dose advantage. This goal is the basis of the present program at Argonne.

Although the dose advantage is sufficient to justify developing such a proton radiographic system, there exists an even stronger justification in terms of providing accurate stopping power measurements of tissue for the charged particle therapy programs. Since the width of the Bragg peak is only a few percent of the range, the stopping power of the intervening tissue must be known to this same precision in order to optimize the treatment procedure. If x-ray CAT scanners are used to calculate the required stopping power for a given treatment, inaccuracies of more

than 10% could arise, even if the chemical composition is accurately known.[10] However, a proton tomographic system could provide the necessary accuracy in situ, with low dose and also ensure that the tumor volume is properly positioned in the field of exposure.

Finally, we would like to draw some additional comparison between the use of protons and x-rays for imaging that may not be commonly known. Although the x-ray source is simple in construction and operation, the x-ray beam is complicated to understand quantitatively due to its polychromatic nature, scattered radiation, and difficulty in detecting. With protons, the source is complicated and more costly but the beam more easily understood quantitatively. Inexpensive detector systems can be built with 100% quantum efficiency, and even coincidence counting can be used to improve signal to noise. Since nuclear interactions occur so rarely, dosimetry measurements for protons can be easier and more accurate than for x-rays. The necessity to measure the transmitted proton flux less accurately than for x-rays decreases the severe requirements on instrumentation accuracy required for x-ray systems. In addition, the ability to steer proton beams magnetically could permit ultrafast CAT scanning without mechanical motion.

Acknowledgments

The proton radiographic data presented here were made possible by the dedicated effort of many people of the Accelerator Research Facilities Division at Argonne National Laboratory. Their work on constructing a unique accelerator facility and on providing the beam to meet our special requirements is greatly appreciated. Our special thanks is due A. R. Passi, R. L. Stockley, and R. E. Timm for providing the beam and data systems for this experiment. We would also like to thank Drs. E. W. Hoffman, R. D. Klem, E. F. Parker, and P. F. Schultz for their help during this program. Finally, we wish to thank Drs. V. W. Steward, L. S. Skaggs, and A. Haus of the University of Chicago for providing the biological specimens, x-ray radiographs, and constant encouragement during this program.

References

1. A. M. Koehler, Science 160, 303 (1968).
2. V. W. Steward and A. M. Koehler, Science 179, 913 (1973); Nature 245, 38 (1973); Radiology 110, 217 (1974).
3. J. A. Cookson, Naturwissenschaften 61, 184 (1974).
4. E. V. Benton et al., Science 182, 474 (1973).
5. K. M. Crowe et al., IEEE Trans. Nucl. Sci. NS-22, 1752 (1975).
6. R. M. Sternheimer, Phys. Rev. 117, 485 (1960).
7. S. L. Kramer et al., work in progress.
8. H. Bichsel, Radiation Dosimetry, F. Attix and W. Roesch, editors, Academic Press, New York (1968).
9. H. E. Johns and J. R. Cunningham, The Physics of Radiology, Charles C. Thomas, Springfield, Illinois (1974).
10. A. M. Koehler et al., Rad. Research 26, 334 (1965).
11. R. Huesman et al., LBL-3040, Lawrence Berkeley Laboratory (1975).
12. K. M. Hanson et al., LA-UR-77-2385, Los Alamos Scientific Laboratory (1977).
13. J. B. Robertson et al., Cancer 35, 1664 (1975).
14. M. R. Raju, LA-5041-MS, Los Alamos Scientific Laboratory (1972).
15. D. R. Moffett et al., IEEE Trans. Nucl. Sci. NS-22, 1794 (1975).
16. G. C. E. Burger, Philips Tech. Rev. 11, 291 (1950).
17. R. L. Martin, Proc. IV All-Union National Conf. on Particle Accelerators, Moscow, USSR, 370 (1975); R. L. Martin et al., IEEE Trans. Nucl. Sci. NS-22, 1802 (1975).

Fig. 1 The transmission curve for 200 MeV protons and 40 keV x-rays in water.

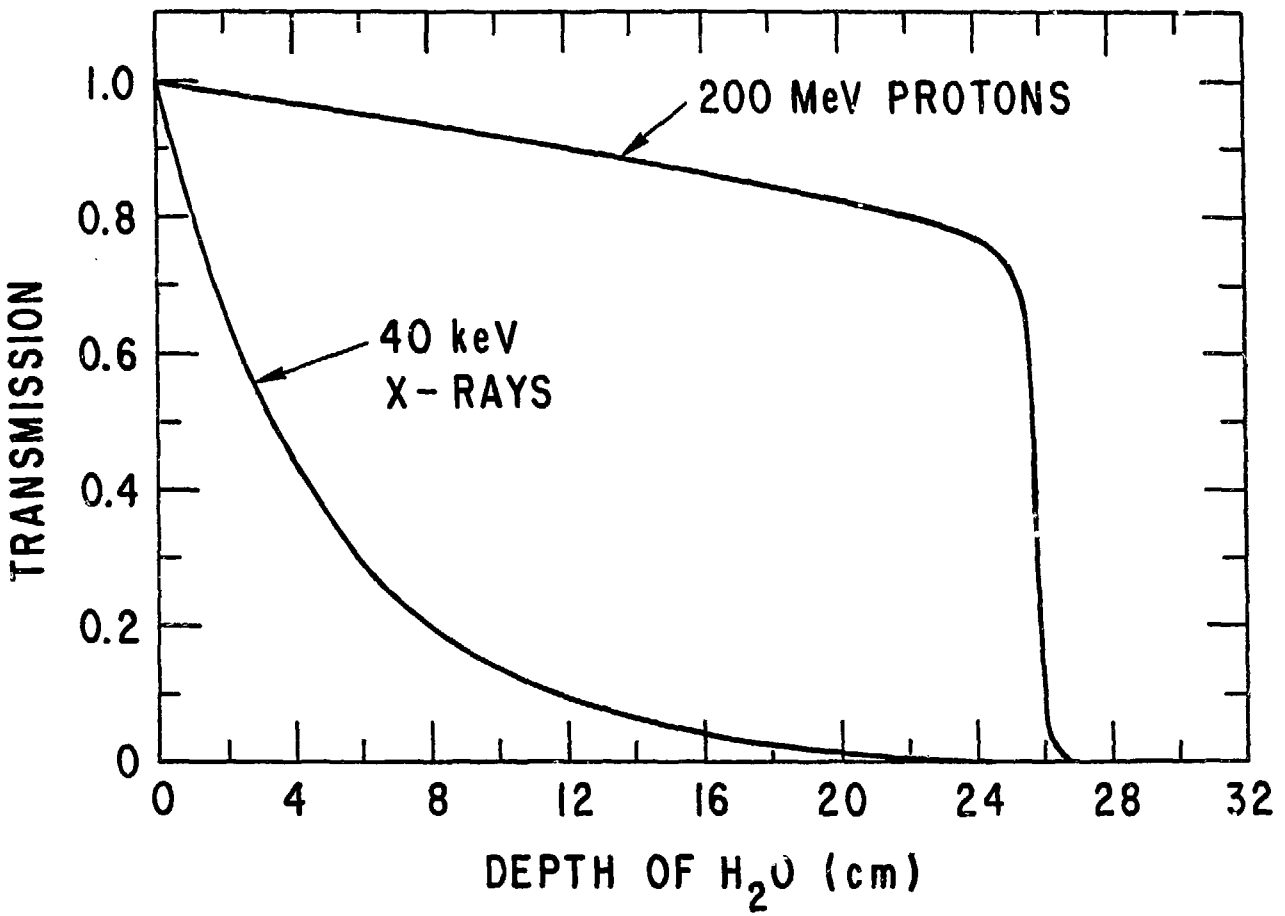

Fig. 2 The stopping power for protons as a function of atomic number (Z) for 100 and 200 MeV. The curve indicates the Z/A dependence of the stable elements. Also shown are the average value and spread about the average stopping power for 100 MeV protons over the elements of biological interest.

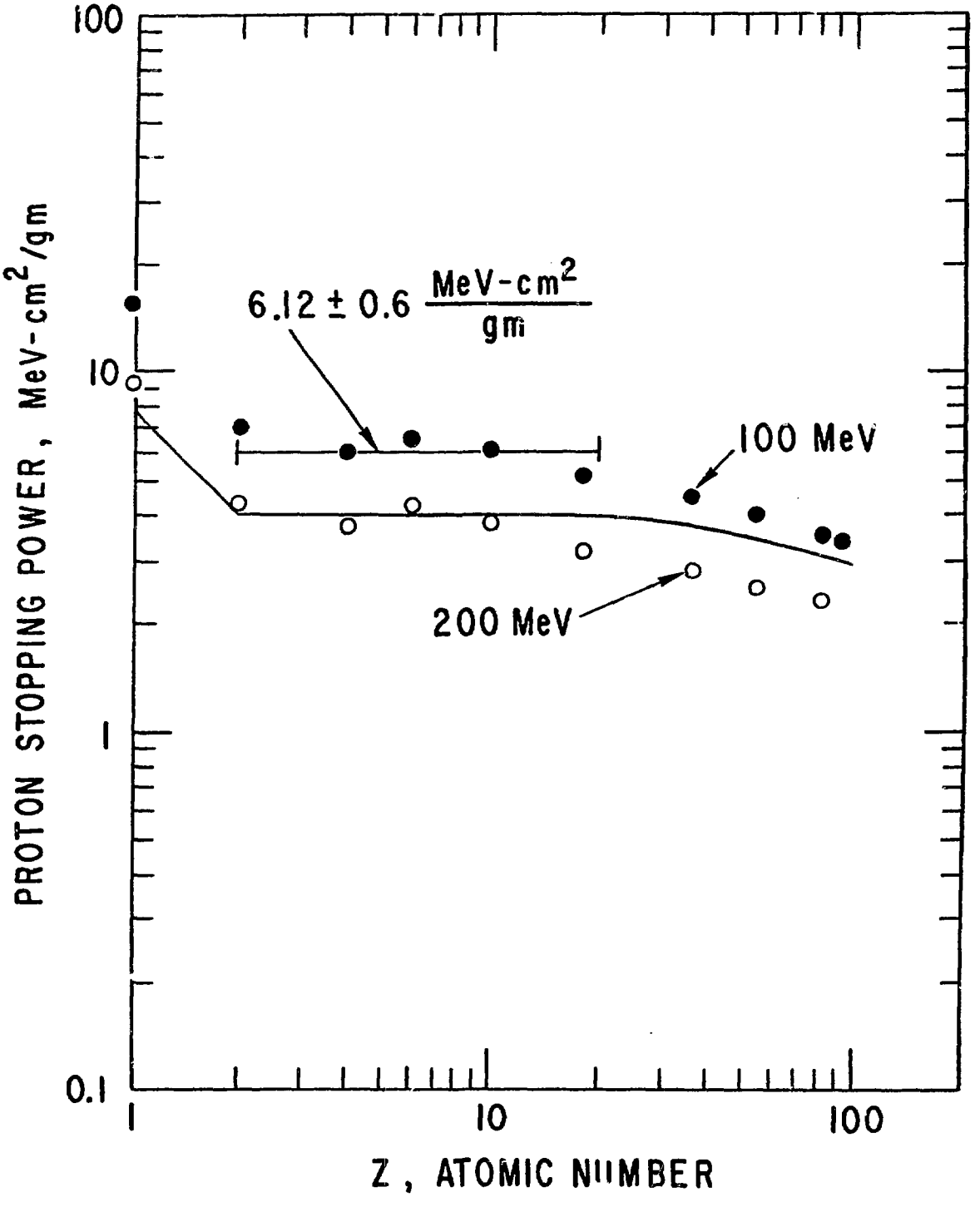

Fig. 3 The mass attenuation coefficient as a function of atomic number (Z) for 40 and 100 keV x-rays.

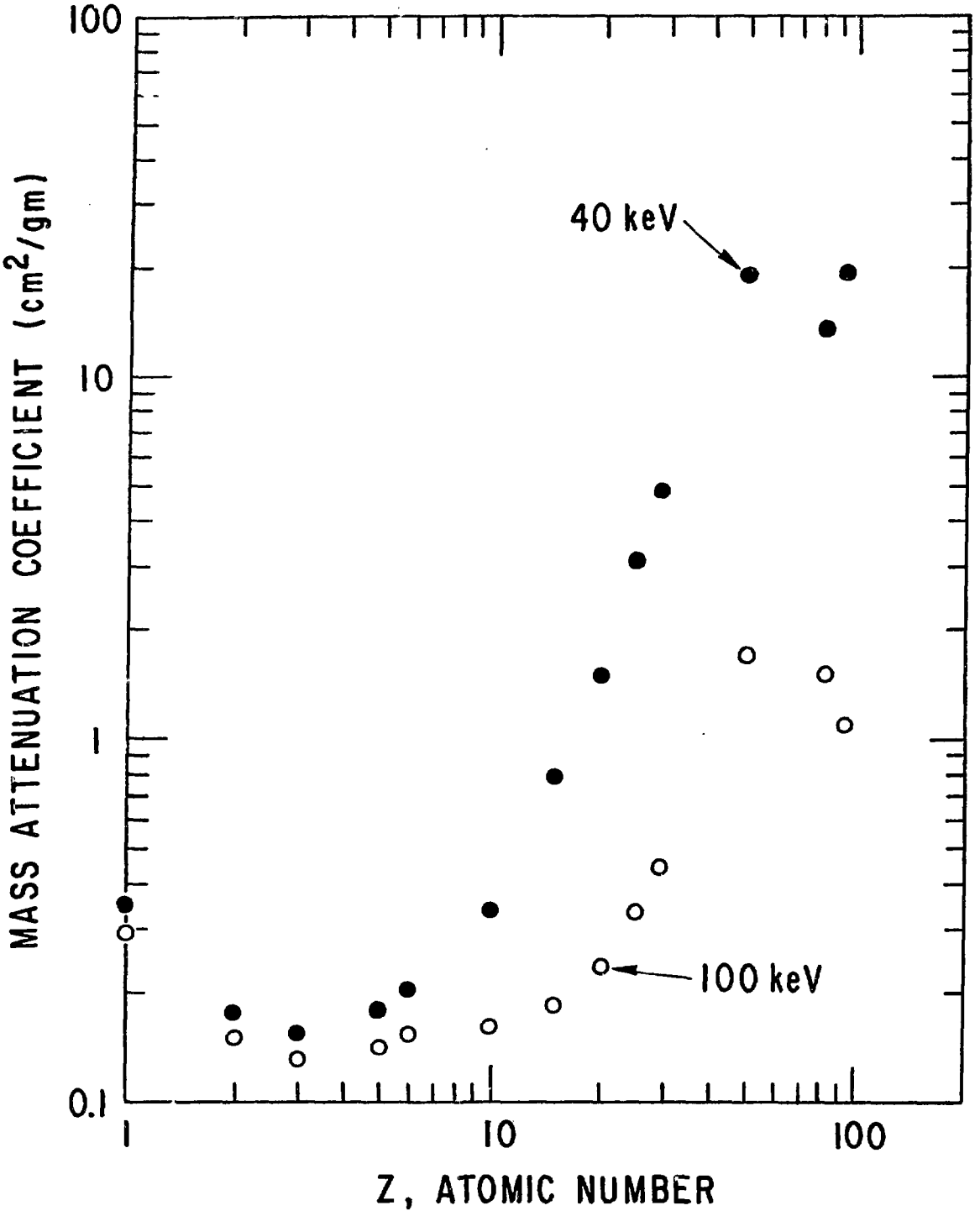

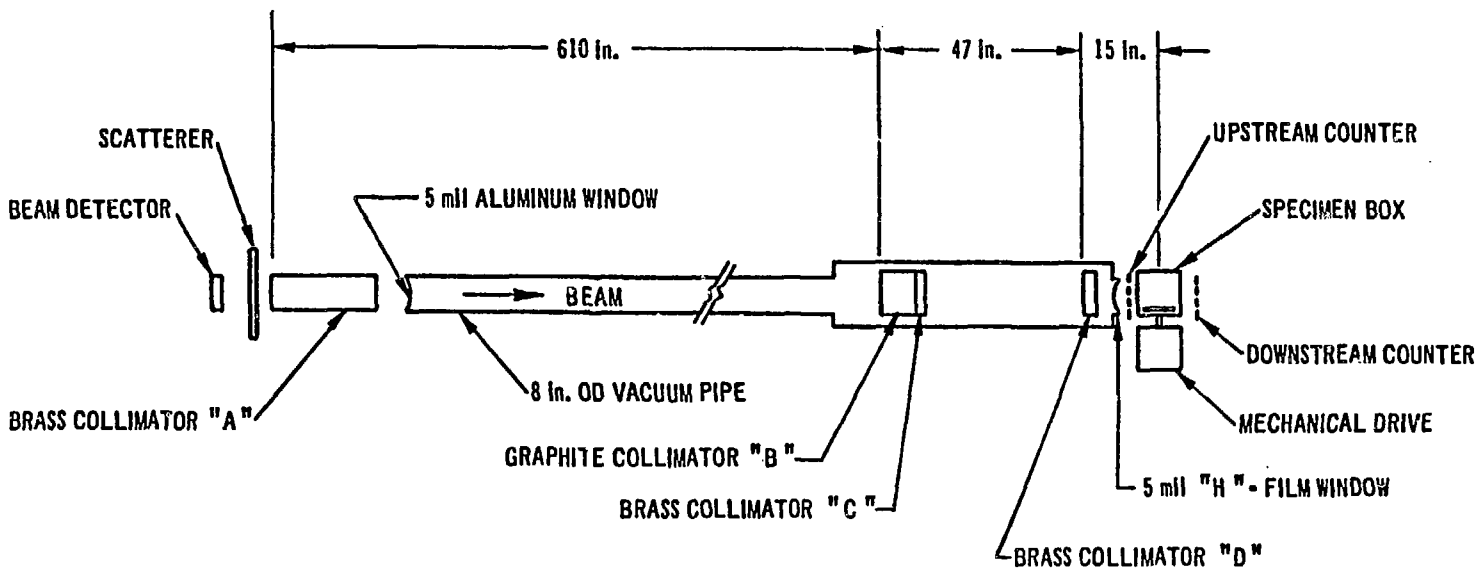

Fig. 4 Schematic of beam transport and collimator system used to obtain the proton radiography data.

Fig. 5 Uncorrected transmission ratio for the four beams resulting from a single horizontal scan of the phantom described in the text.

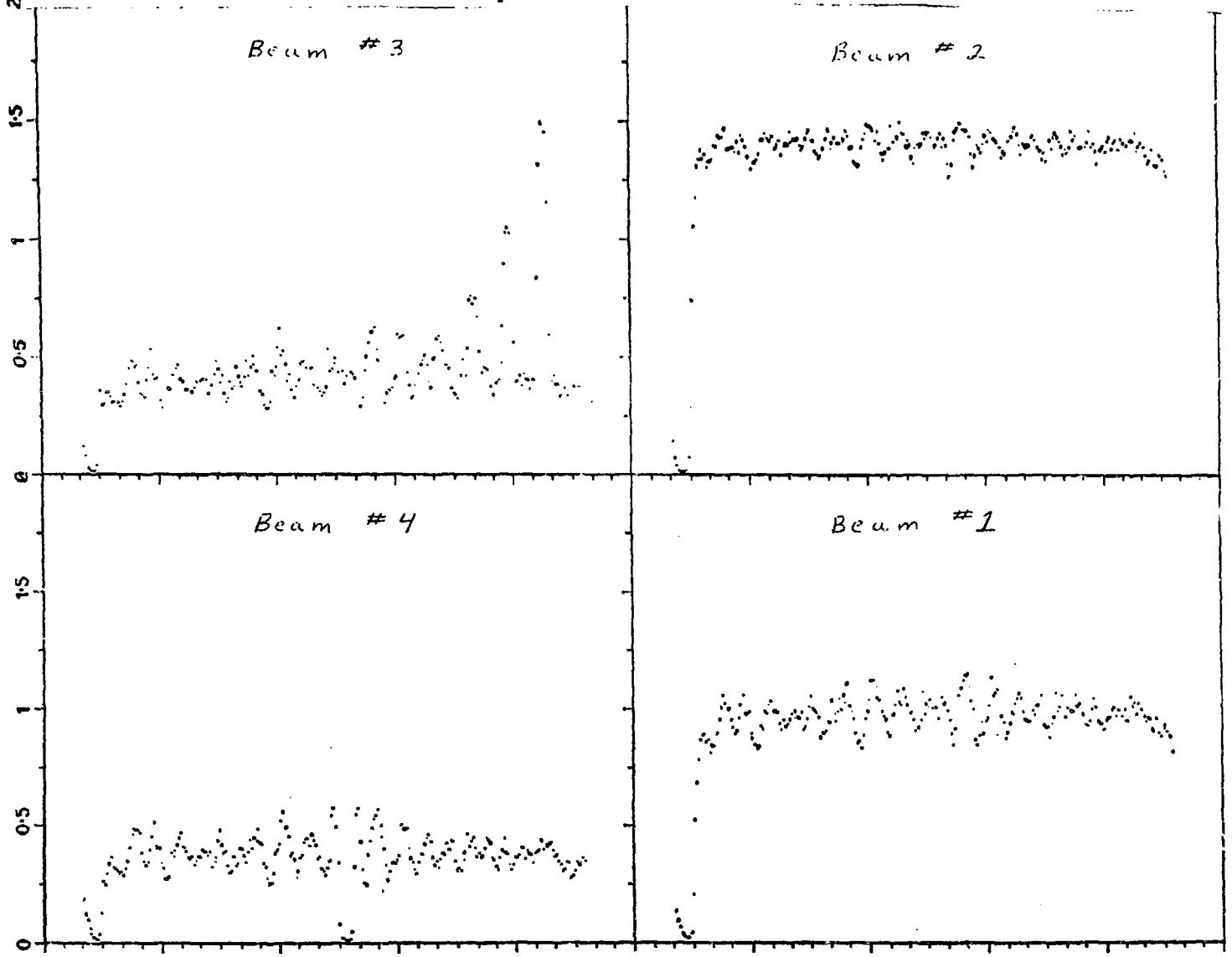

Fig. 6 Transmission ratio for the scan lines presented in Fig. 5, corrected for the energy fluctuations using beam number 1.

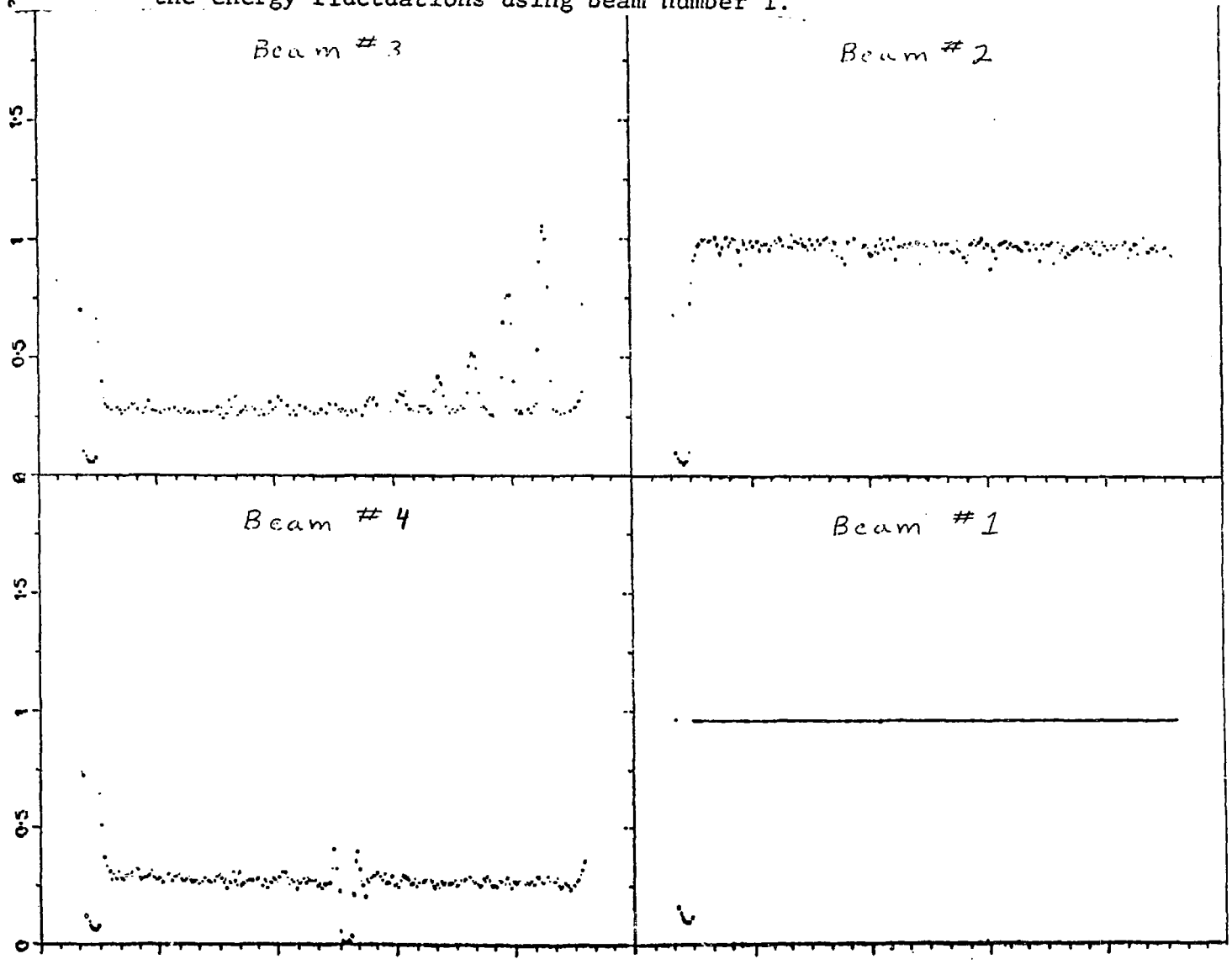

Fig. 7

A proton shadowgraph of the visibility phantom described in the text. The shaded bar to the right shows the display window with the numbers indicating the range in mass (g/cm^2) measured by the proton beam less the 24.8 g/cm^2 for the water box; (a) 0.8166 to 2.2994 g/cm^2, (b) 1.3109 to 1.8051 g/cm^2, and (c) 1.5 to 1.7 g/cm^2.

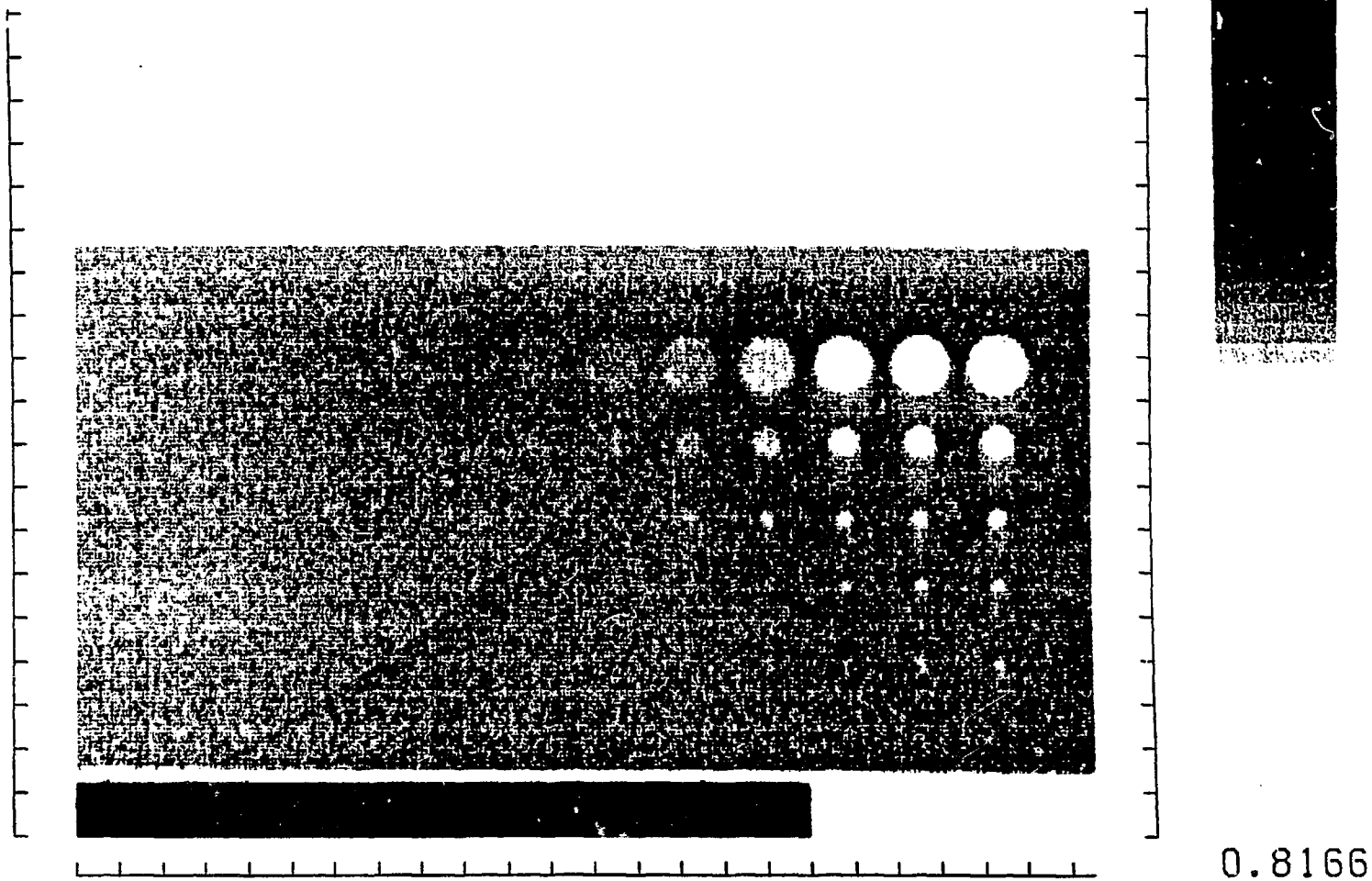

Fig. 7(a)

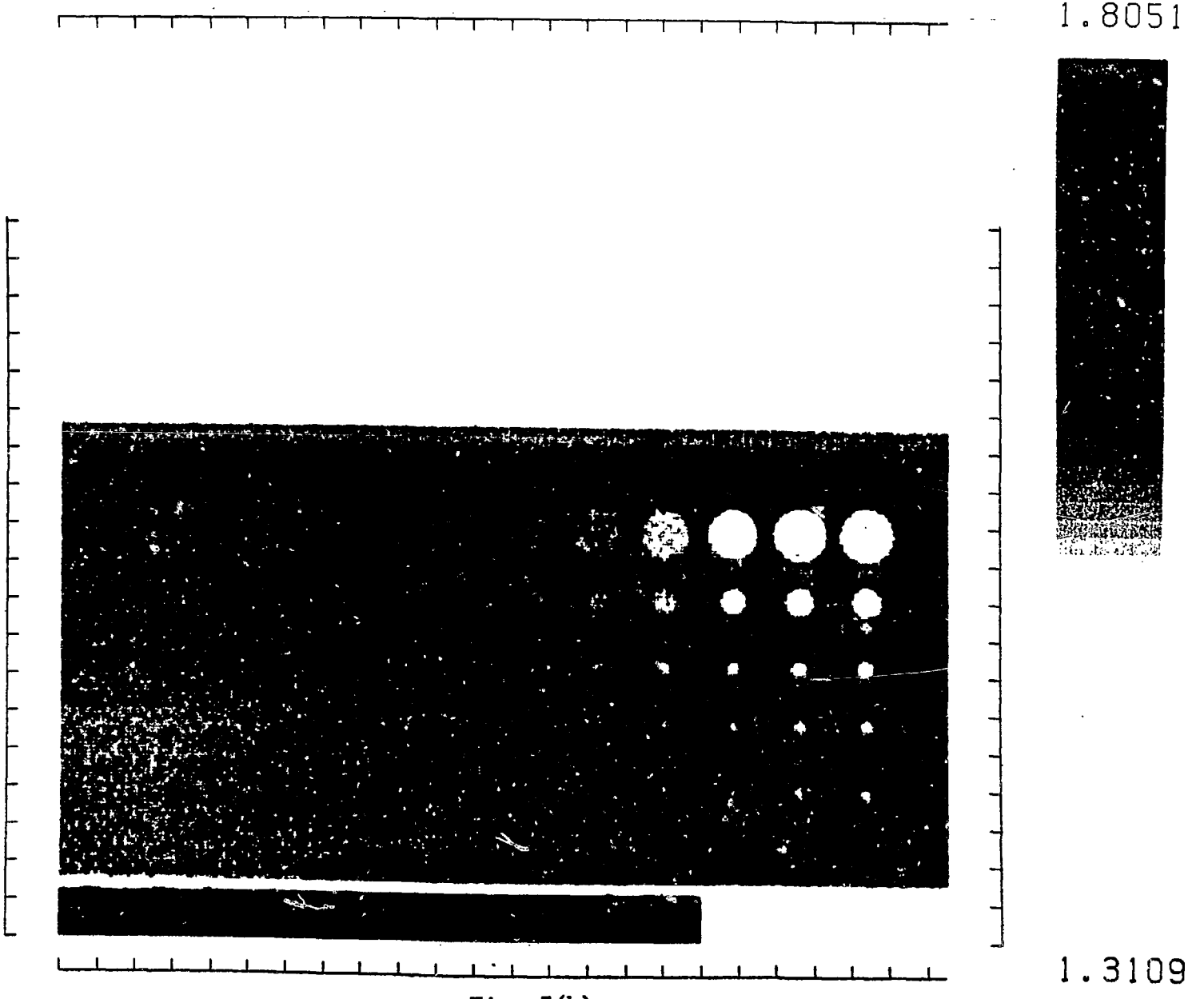

Fig. 7(b)

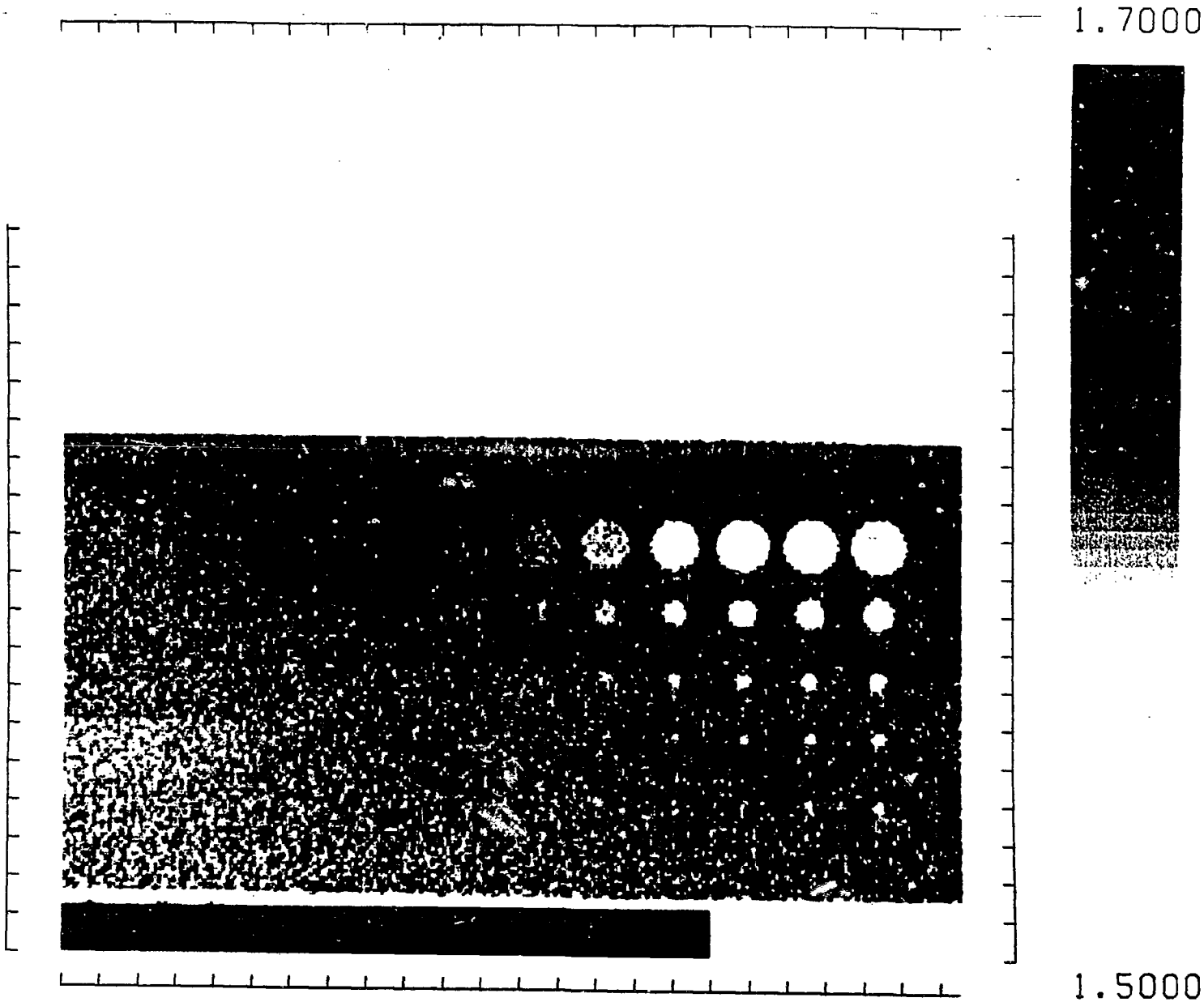

Fig. 7(c)

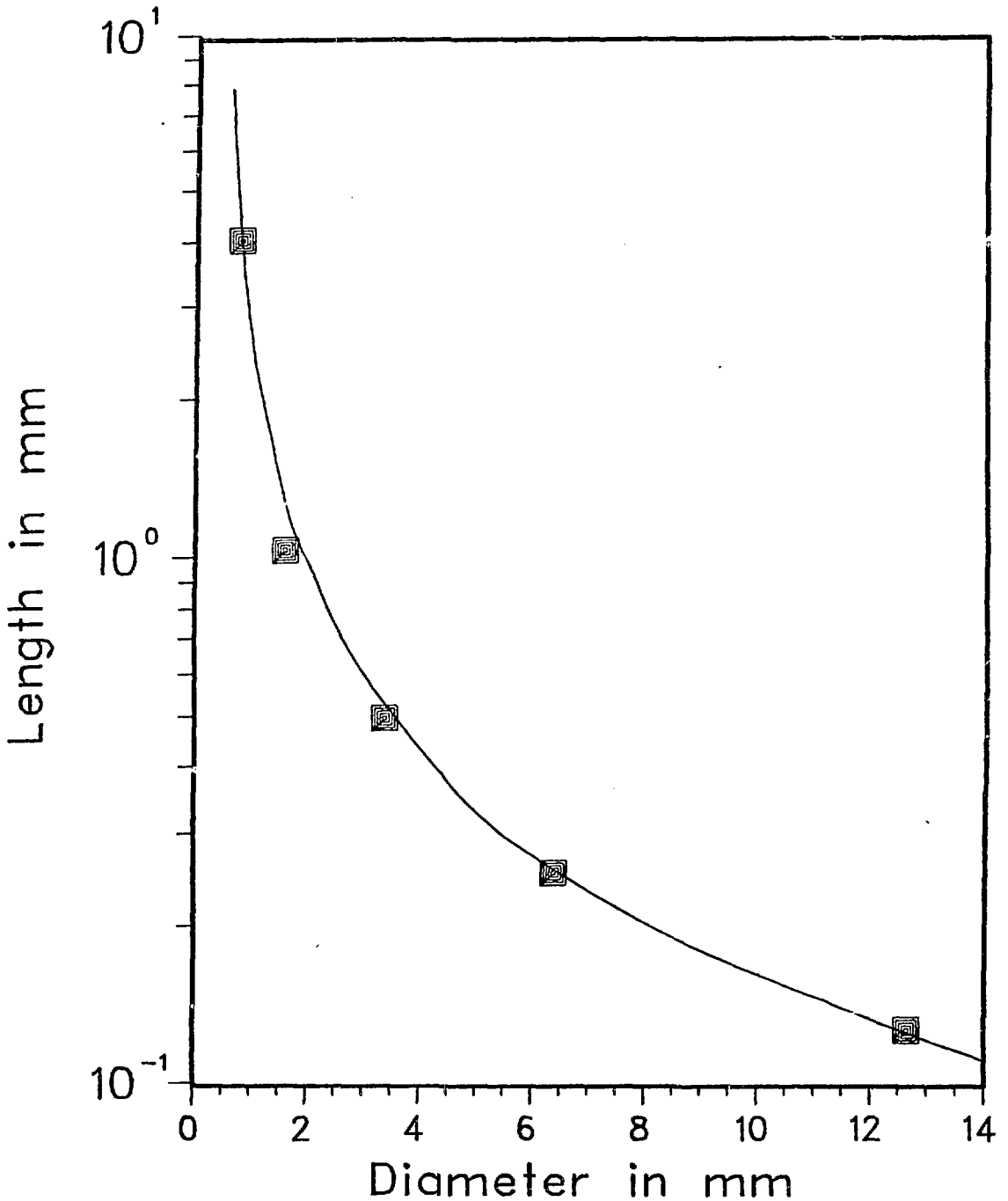

Fig. 8 The minimum visible length (contrast) hole as a function of the hole diameter for the proton shadowgraph in Fig. 7. The curve is an attempt to describe the visibility data assuming a constant signal-to-noise ratio modified by the finite beam size.

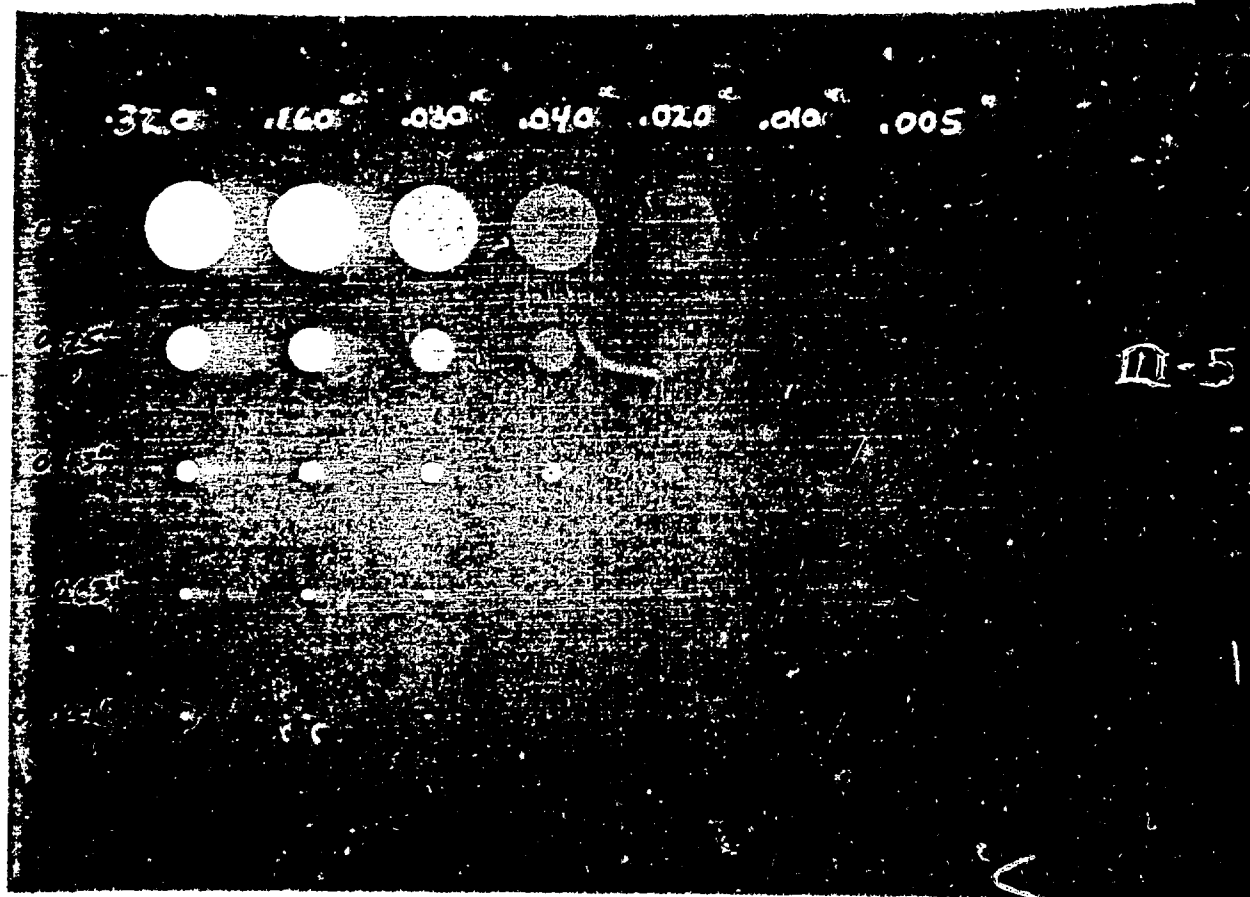

Fig. 9 The x-ray shadowgraph of the phantom in Fig. 7 but without the 24 cm water bath used for the proton shadowgraphs.

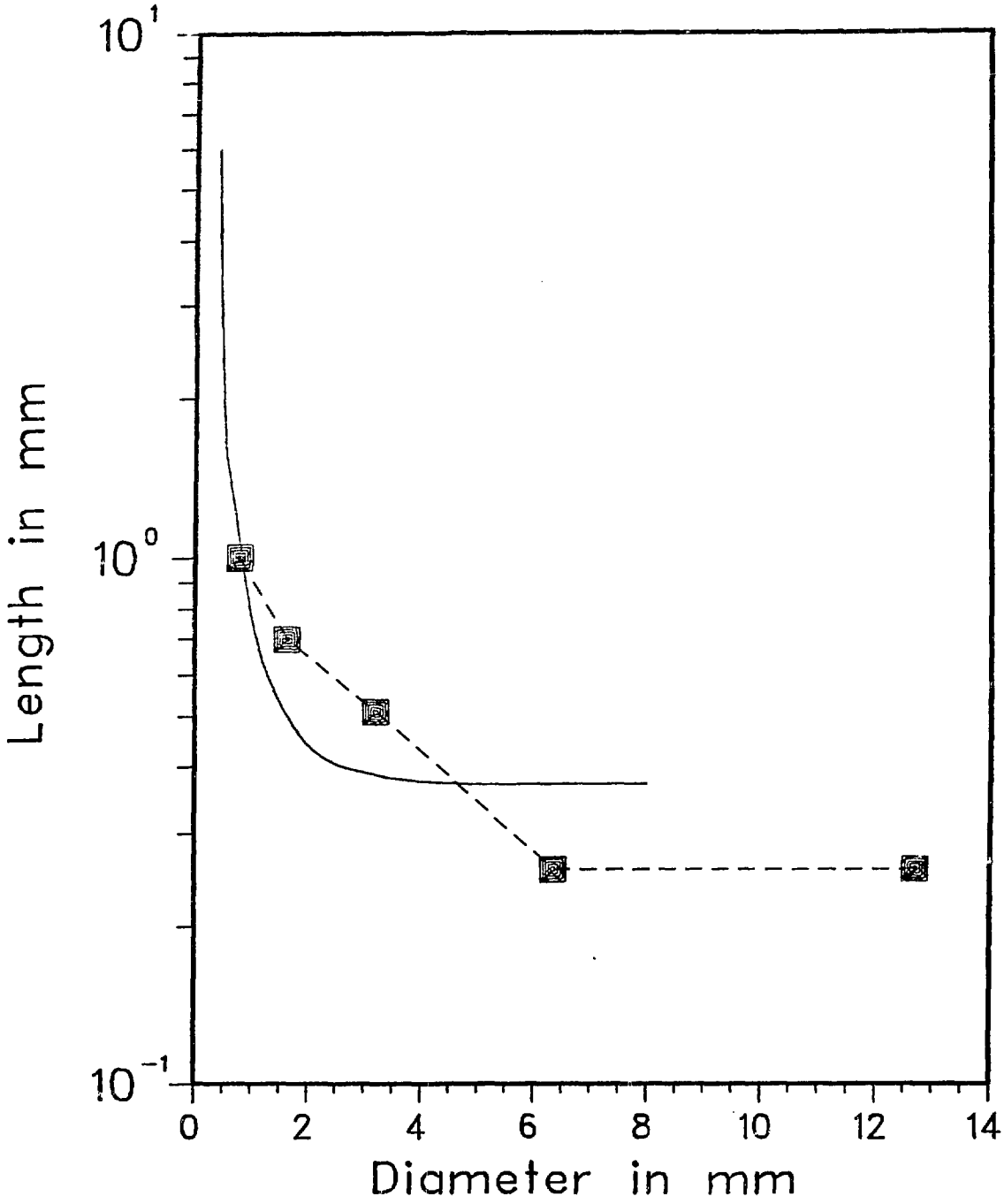

Fig. 10 The visibility data for the x-ray shadowgraph in Fig. 9. The solid curve is the result of a more detailed study described in Ref. 16.

1.6189

Fig. 11 A proton shadowgraph of a radical mastectomy with metastatic carcinoma. The display windows are (a) 0.9385 to 1.6189 g/cm^2, (b) 1.1 to 1.5 g/cm^2, and (c) 1.2 to 1.6 g/cm^2. The white marks in the center are air bubbles in the water box.

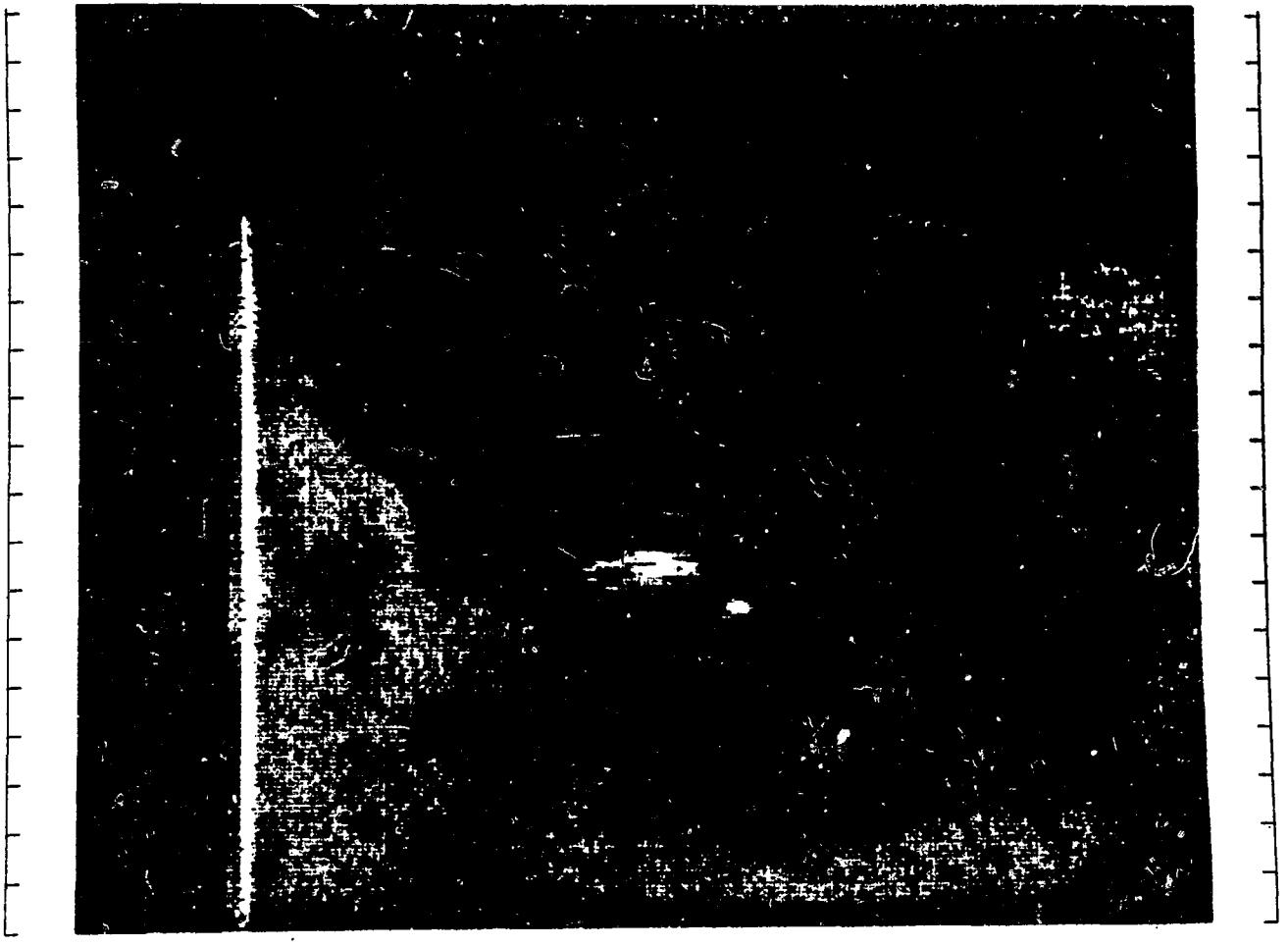

Fig. 11(a)

0.9385

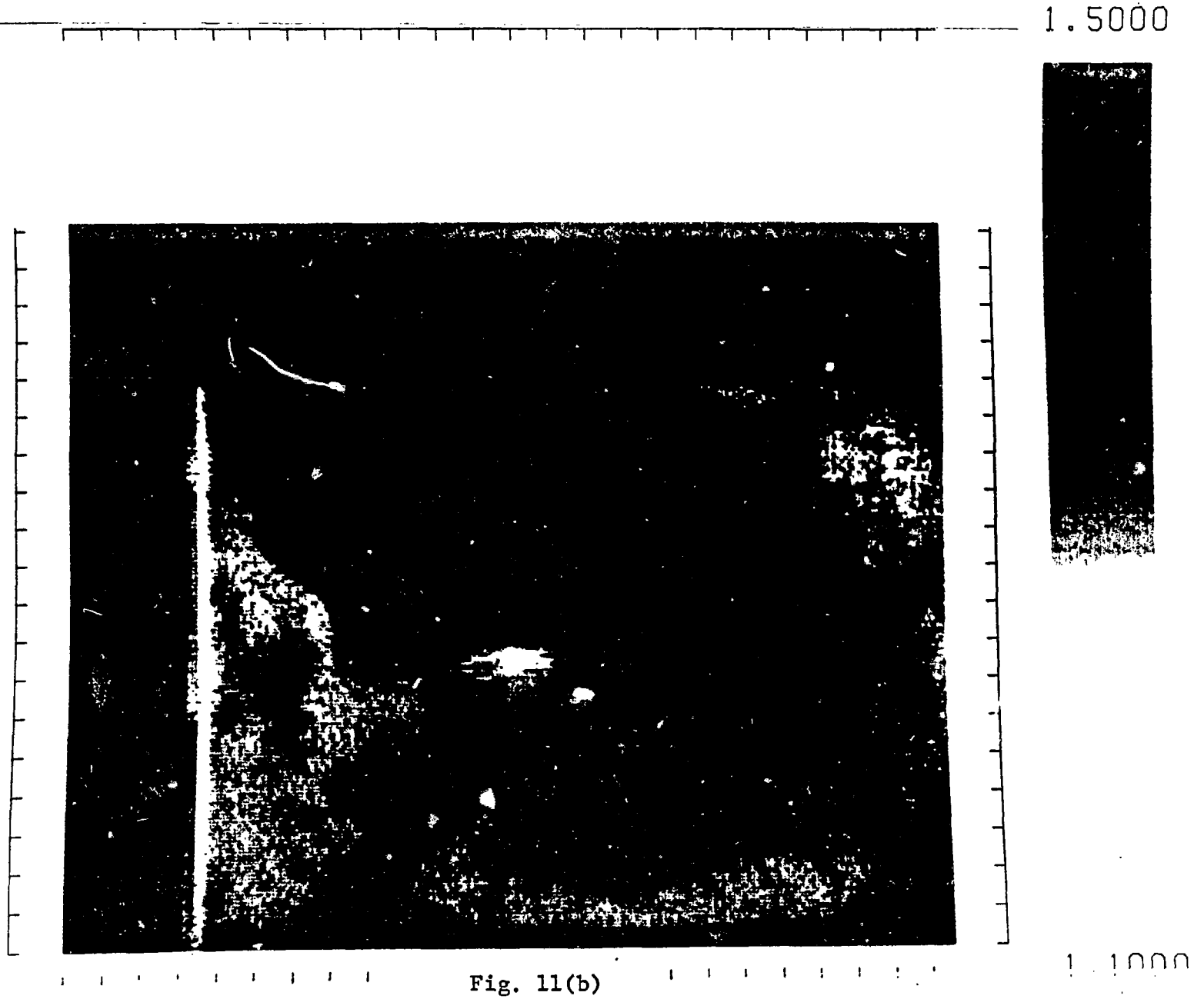

Fig. 11(b)

Fig. 11(c)

Fig. 12 The x-ray mammograph of the same breast in Fig. 11. The radiographs were taken in two halves and joined together.